Journal of Materials Chemistry A

COMMUNICATION

Better than crystalline: amorphous vanadium oxide for sodium-ion batteries†

E. Uchaker, Y. Z. Zheng, S. Li, S. L. Candelaria, S. Hu and G. Z. Cao*

Cite this: *J. Mater. Chem. A*, 2014, **2**, 18208

Received 22nd July 2014
Accepted 10th September 2014

DOI: 10.1039/c4ta03788j

www.rsc.org/MaterialsA

Amorphous and nanocrystalline vanadium pentoxide (V_2O_5) were prepared through a combination of sol–gel processing paired with electrochemical deposition and investigated as cathodes for sodium-ion batteries. Amorphous V_2O_5 demonstrated superior electrochemical properties upon sodiation as compared to its crystalline counterpart. More specifically, amorphous vanadium pentoxide had a measured capacity of 241 mA h g^{-1}, twice the capacity of its crystalline contemporary at 120 mA h g^{-1}. In addition, the amorphous vanadium pentoxide demonstrated a much higher discharge potential, energy density, and cycle stability. The development of amorphous materials could enable the usage and design of previously unexplored electrode materials; herein, the possible relationship between the improved sodiation properties and the amorphous structure is discussed.

The progress of energy storage materials and devices appreciably lags the rapid progression of other electronic components in spite of the steady advancements in these technologies, and has increasingly become a bottleneck impeding device development.[1,2] Among commercially available energy storage media, lithium-ion (Li-ion) batteries constitute a mature and robust technology and are extensively used in consumer devices because of their high energy density and portability.[3–6] Despite great commercial success, lithium-based batteries have several drawbacks associated with their use, such as potential safety issues, high cost, and resource scarcity. Conversely, sodium-ion batteries (Na-ion) have been gaining considerable traction as a realistic candidate for large-scale energy storage applications over the past several years.[7–9]

Na-ion batteries are attractive because sodium resources are seemingly inexhaustible, as well as ubiquitous, and therefore cost considerably less (by a factor of roughly 30–40 times) than lithium. Moreover, sodium does not undergo an alloying reaction with aluminum at low voltages, as is the case with lithium, meaning that aluminum can replace copper as the anodic current collector, which equates to an overall cell cost savings of ~2%.[10–12] The lower operating voltage of Na-ion cells results in enhanced stability of the non-aqueous electrolyte,[11] but also manifests itself in a lower energy density. The majority of the proposed electrode materials for Na-ion batteries show similar or slightly lower specific capacity and redox potential than when used in Li-ion cells.[13,14] Moreover, the accommodation of sodium in traditional host materials is difficult because the ionic radius and reduction potential of sodium are strikingly larger than that of lithium.[15] Therefore, the de/sodiation process induces large distortions in the host lattice that ultimately lead to pulverization of the electrode and the impending failure of the cell.

Crystalline materials have been the primary electro-active species of choice in the battery field for some time now, but their synthesis can be time-consuming, energy intensive, and costly. It has recently been demonstrated that disordered materials may form percolation pathways *via* the opening of active diffusion channels that could potentially facilitate ionic diffusion;[15,16] moreover, several studies have revealed that Li-ion diffusion in amorphous materials proceeds more rapidly than in crystalline materials with similar particle size and morphology.[17] Based on these considerations, it is worth investigating amorphous or structurally disordered transition metal oxides because of their isotropic characteristics that may enhance Na-ion diffusion by offering diffusion paths that are not highly anisotropic, as is the case for crystalline materials.[18] Short-range ordered materials may also have a lower entropic energy associated with the ordering of incorporated ions, and a more open framework to facilitate ionic transport. In this sense, it is possible to describe amorphous materials as homogeneously disordered, in terms of anisotropy and potential defects, and crystalline materials as heterogeneously disordered.

Vanadium oxide is an attractive multifunctional material used in widespread applications in various fields, such as catalysis,[19] energy storage,[20,21] and biomedical devices;[22] a wide

Department of Materials Science & Engineering, University of Washington, Seattle, WA, USA. E-mail: gzcao@u.washington.edu

† Electronic supplementary information (ESI) available: Experimental methods, N_2 isotherms, TGA, TEM, XPS, XAS, and CV available online. See DOI: 10.1039/c4ta03788j

assortment of V_2O_5 nanostructures have already been synthesized by a variety of methods.[23–26] For Li-ion battery applications, the intercalation of lithium into V_2O_5 has been well documented and occurs with compensating electrons leading to the formation of vanadium bronzes; however, reports concerning the use of vanadium oxide for sodium-based energy storage systems are limited. Tepavcevic *et al.* demonstrated that the deintercalation of bilayered V_2O_5 electrodes was accompanied with the loss of long-range order, while short-range order was preserved. The bilayered V_2O_5 cathodes were able to maintain 85% of their initial capacity after 350 cycles, with the current density varying from 20–630 mA g^{-1}.[27] Bilayered V_2O_5 nanobelts with a comparable performance have also been reported more recently.[28] NaV_6O_{15} nanorods have shown moderate capacity values but poor retention,[29] while V_2O_5-based Na-ion pseudo-capacitors have delivered a maximum specific energy of 40 W h kg^{-1} and retained 80% of their original capacity after 900 cycles at a 60 C discharge rate.[30] However, a study concerning amorphous vanadium oxide has yet to be reported. Herein, we detail the electrochemical deposition of V_2O_5 using vanadium-based gels and their application in Na-ion batteries.[31,32] The amorphous V_2O_5 electrode displayed superior electrochemical performance compared to its crystalline counterpart, readily demonstrating that the use of amorphous materials may be of considerable value for future electrode design, pending further optimization.

The method used for V_2O_5 gel preparation was adopted from previous work, and involved several parallel and sequential chemical reactions, as described in the ESI†.[33] Ultimately, hydrous vanadium oxide was deposited through the electrochemical deposition of VO_2 and the catalyzed gelation of V^{4+}, which served as a nucleation center that initiated and catalyzed the formation of $V_2O_5 \cdot nH_2O$. Following the electrochemical deposition on Ni-foil, the electrodes were processed under different thermal treatment conditions: ambient (as-processed), 180 °C under vacuum (180 °C vac) for 3 hours, and 450 °C in air (450 °C air) for 3 hours. These temperatures and atmospheres were chosen based on previous results showing that V_2O_5 initiates crystallization at approximately 216 °C.[34] The main reason for annealing under vacuum at 180 °C is to remove a considerable amount of the crystalline water, while preserving the amorphous homogeneity and suppressing crystallization.

The morphology of the films was observed by scanning electron microscopy (SEM), a representative image of which is shown in Fig. 1. SEM reveals that the V_2O_5 was homogenously deposited and composed of layers stacked parallel to the substrate that are composed of irregularly shaped nanoparticles with an average size of 500 nm. The layered structure is a product of the deposition process, which took place through a combination of cathodic deposition and catalyzed gelation, and imparts a significant degree of structural stabilization unto the sample.[23,31,32] The overall morphology of the various samples did not differ significantly with thermal treatment, but the observed roughness did increase with temperature. The slight increase in roughness is most likely caused by minor coarsening effects brought on by exposure to higher temperatures.

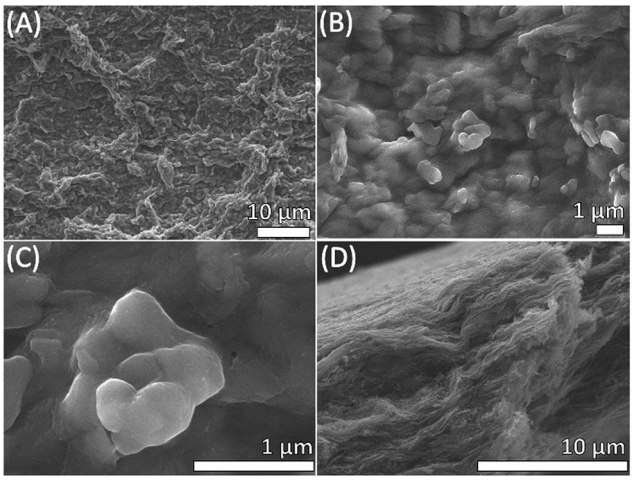

Fig. 1 Representative SEM images of V_2O_5 films deposited on Ni-foil for one hour: (a and b) low-resolution, (c) high-resolution, and (d) cross-sectional images.

Nitrogen adsorption–desorption isotherms were collected, in order to evaluate the surface area and pore characteristics. The Barrett–Joyner–Halenda (BJH) pore size distributions (Fig. S1†) obtained from the isotherms suggest that the 180 °C vac and 450 °C air annealed samples contain broadly distributed pores, the majority of which are smaller than 15 nm, with a respective average pore size of 3.22 and 3.19 nm; the overall pore volumes were nearly identical as well. The Brunauer–Emmett–Teller (BET) derived specific surface areas were 38.7 and 32.6 m^2 g^{-1}, respectively, confirming that the varying thermal treatments had little change on the morphology outside of the slight coarsening and surface roughening effects.

The crystallinity of the samples was initially assessed using X-ray diffraction (XRD, Fig. 2a). The 450 °C air annealed specimen could be indexed to the orthorhombic form of vanadium pentoxide, V_2O_5 (space group: *Pmmn* (59), $a = 11.516$, $b = 3.566$, $c = 3.777$ Å; JCPDS card no. 41-1426), with no detectable impurities or secondary phases. There were no detected peaks in the as-processed and 180 °C vac samples. The lack of any diffraction peaks serves as a strong indication and confirmation of their amorphous quality, and this was further confirmed by TEM, Fig. S2.† However, the XRD spectra offer little information in terms of bonding, coordination, and chemical identification. Fourier transform infrared (FTIR, Fig. 2b), X-ray photoelectron (XPS, Fig. 2c), and X-ray absorption (XAS, Fig. 2d) spectroscopy were therefore conducted in order to reliably distinguish the chemical nature and structural characteristics of the different specimens.

FTIR was utilized to chemically identify the seemingly amorphous compounds. As shown in Fig. 2b, the absorption peak stemming from the symmetric stretching mode of the vanadyl V=O bond is observed at approximately 1012 cm^{-1} for all the samples. However, the same stretching vibration was shifted to a slightly higher value (1019 cm^{-1}) for the 450 °C air sample. For the as-processed and 180 °C vac samples, the peaks localized at 767 and 532 cm^{-1} are assigned to the 3-fold-coordinated oxygen asymmetric and the symmetric stretching

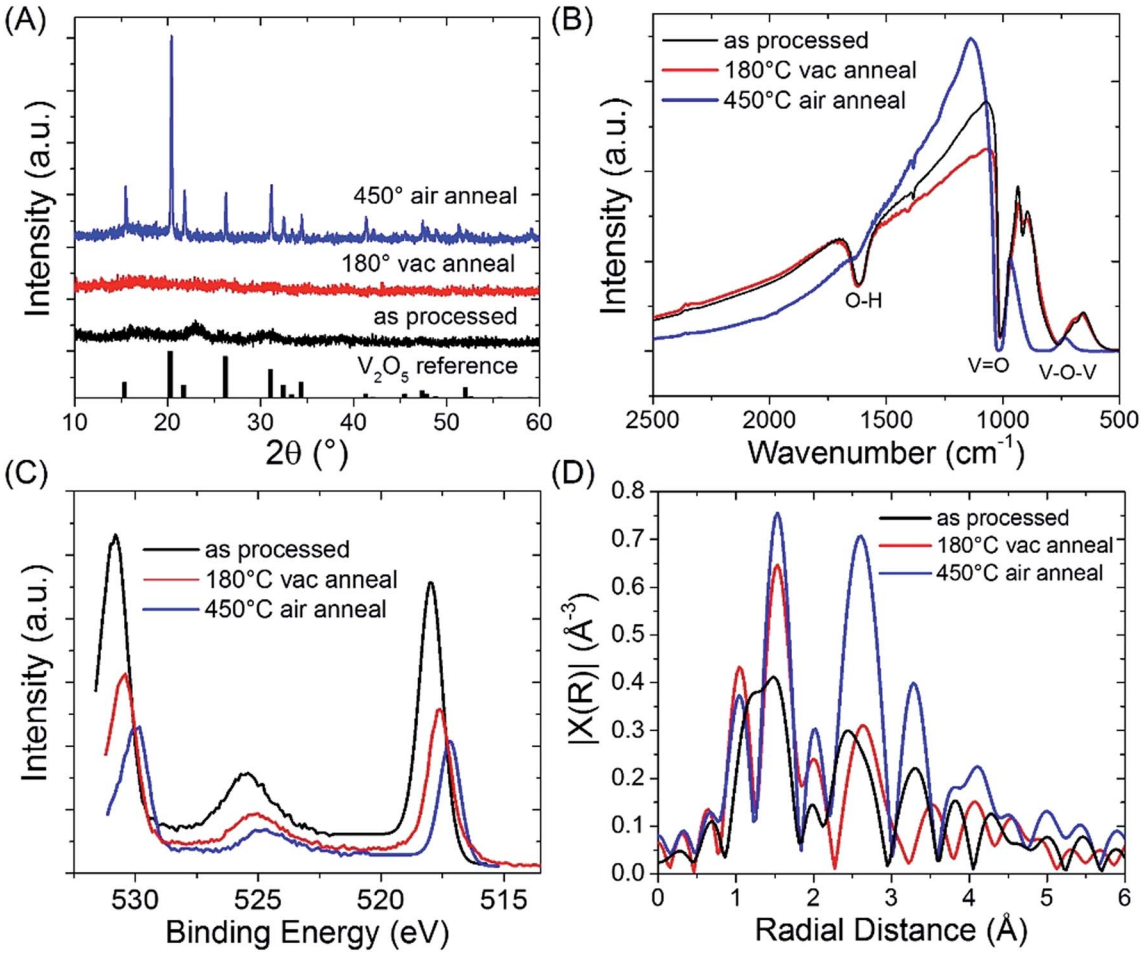

Fig. 2 (a) XRD patterns, (b) FTIR spectra, (c) high-resolution XPS spectra, and (d) k^3-weighted Fourier transform of the V k-edge EXAFS of the V_2O_5 samples.

vibrations modes of V–O–V, respectively. The lack of a long range crystallographic order in the samples thermally treated at lower temperatures leads to a homogeneously disordered material, and is ultimately accountable for the wide distribution and shifting of the peaks at lower wavenumbers.

The FTIR absorption peak at 1615 cm^{-1} is assigned to the hydroxyl group (O–H) stemming from absorbed water and is also not detected in the fully crystallized material.[35] The incorporation of crystalline water may account for some of the disparity among the vibration modes;[36,37] thus, water molecules incorporating themselves within or on the surface of the amorphous material can effectively alter the ionic transport pathways.[38,39] It has been demonstrated for $V_2O_5 \cdot nH_2O$ xerogel that the presence of water molecules can expand the interlayer distance, which correspondingly enhances the intercalation capacity as a result.[40] This modification is usually detected by XRD, where the (100) peak will shift from its standard value ($2\theta = 20.258°$) to a lower value ($2\theta \approx 8°$), but this fact cannot be used in this investigation given the amorphous nature of the 180 °C vac sample. Consequently, such effects can lengthen the bond distance and decrease the strength of the V═O bond, while simultaneously strengthening the 3-fold-coordinated V–O–V bond, leading to the shift in the detected bond vibrations. These spectra match well with those for amorphous V_2O_5 previously reported in the literature.[34,35,37] The amount of water in the samples was examined using thermogravimetric analysis (TGA), and was quantified at approximately 12% and 0.4% for the vacuum and air annealed materials, respectively (Fig. S1c†). These results were substantiated by bulk density measurements, using the specific gravity method that measured the density of the 180 °C vac and 450 °C air materials to be 2.1 and 2.7 $cm^3\ g^{-1}$, respectively. XAS results elucidated the location of the water, and will be covered later.

XPS was carried out on the samples prior to sodiation, in order to obtain more information on the chemical state of the vanadium species present and for additional phase identification. High-resolution scans, emphasizing the V2p and O1s peaks, and broad survey scans were collected, and are shown in Fig. 2c and S3,† respectively. All materials were indexed as V_2O_5 with the only vanadium species present being V^{5+}. The trends between the peak position, peak spacing, and their literature comparisons are shown graphically in Fig. S3 and numerically in Table S1.† Slight shifts in the peak positions were attributed to the lack of long-range order and the homogeneously disordered makeup of the structure. The V_2O_5 phase was confirmed by the spin–orbit splitting of approximately 7.5 eV between the

$V2p_{3/2}$ and $V2p_{1/2}$ orbitals and the energy difference of 12.9 eV between the binding energy of the $V2p_{3/2}$ and the O1s orbitals for all of the samples. These findings are consistent with literature reports.[41–43]

XAS was carried out in transmission mode at the Advanced Photon Source, sector 13ID-E, and the data-sets were processed using the IFFEFIT software package.[44] The normalized extended X-ray absorption fine structure (EXAFS) and V k-edge X-ray absorption near edge structure (XANES) plots are shown in Fig. 2d and S4,† respectively. The pre-edge peak in the XANES spectra corresponds to the 1s to 3d electronic transition, for which the position and intensity are very responsive towards the crystal field symmetry surrounding the vanadium and the distortion of the local structure, as it influences the degree of hybridization between the O2p and the V3d orbitals.[34] A decrease in the pre-edge peak intensity suggests an increase in the vanadyl V=O distance, which decreases the degree of distortion of the local structure and effectively increases the local symmetry within the VO_5 square pyramid.[45,46] The absorption edge itself is associated with the 1s to 4p dipole transition. Comparison of the crystalline and amorphous absorption spectra further verifies that both the thermally treated specimens are in fact V_2O_5.

The k^3-weighted Fourier transform of EXAFS can provide information on the coordination shell distance between atomic neighbors. The direct comparison of the crystalline and amorphous Fourier transforms (see Fig. 2d) displays the radial structure functions for the central absorbing vanadium atom and highlights the variation in the local structures. The amplitude of the peaks for the 180 °C vac material is lower than that of the 450 °C air material, indicating a higher degree of structural disorder and diminished extending coordination.[47,48] The experimental data for the crystalline material shows three well-defined peaks at 1.50, 2.70, and 3.25 Å that are derived from the V–O single scatter contribution (1st coordination sphere), V–V (2nd sphere), and V–V (3rd sphere), respectively. As expected, the intensity of these peaks drops with increasing coordination because of the increased scattering events. The amorphous material shows similar first and second degree coordination, but drastic differences in the third. This is also expected, provided that the amorphous structure lacks long range order, and the third shell contains contributions from a large number of overlapping single, as well as multiple-scattering, contributions. Moreover, the 180 °C vac spectrum is extremely similar to the others gathered for amorphous V_2O_5, as presented in the literature.[34,46] The manifestation of this diminished coordination would be a more open structure, which would be conducive towards improved sodiation. Based on these results, it is probable that the majority of the water detected by TGA corresponds to surface adsorbed water. If anything, the water will add to the disorder between neighboring domains, which could potentially expand the pathways for Na-ion transport.

The storage performance of the electrochemically deposited V_2O_5 was investigated as a Na-ion battery positive electrode candidate using a half-cell configuration. However, prior to this, the 450 °C air annealed V_2O_5 was tested as a Li-ion battery cathode, in order to establish a baseline merit of performance. Lithium and sodium ion batteries function in a matching manner to one another, with the main differences being the reduction potential, ionic size, and electronegativity of the alkali species. The results of this initial baseline test (Fig. S5a†) verified the high electrochemical capability of the 450 °C air annealed material towards lithium, and hence, substantiated its use in this study.

Following this baseline test, the 450 °C air and 180 °C vac materials were cycled against Na/Na^+ at 23.6 mA g^{-1} (0.1 C), the results of which are shown in Fig. 3a and b, respectively. When cycled against Na/Na^+, the crystalline 450 °C air V_2O_5 electrode demonstrated a substantial potential drop, followed by a moderate discharge plateau at approximately 2.3 V and a discharge capacity of approximately 120 mA h g^{-1}. Contrary to its crystalline form, the 180 °C vac material featured a smooth discharge profile, concurrent with the evolution of sodium-ion incorporation, and culminating in a discharge capacity of approximately 241 mA h g^{-1}. The energy density of the amorphous material (625.3 W h kg^{-1}) was also markedly greater than that of its crystalline contemporary (282.6 W h kg^{-1}).

The rate performances of the crystalline (Fig. 3c) and amorphous (Fig. 3d) materials were also investigated. Again, the amorphous V_2O_5 outperformed its crystalline associate. Based on the discharge profiles, the absence of a phase transformation in the amorphous material during Na-ion incorporation can potentially be ascribed to the combination of intercalation and pseudo-capacitive behavior over a wide range of compositions, which leads to an improved reversible cycling performance. Diffusion in disordered materials can be facile, because the percolation of certain diffusion channels become active, thus effectively opening a new avenue for the design of disordered or amorphous electrode materials with high capacity and energy

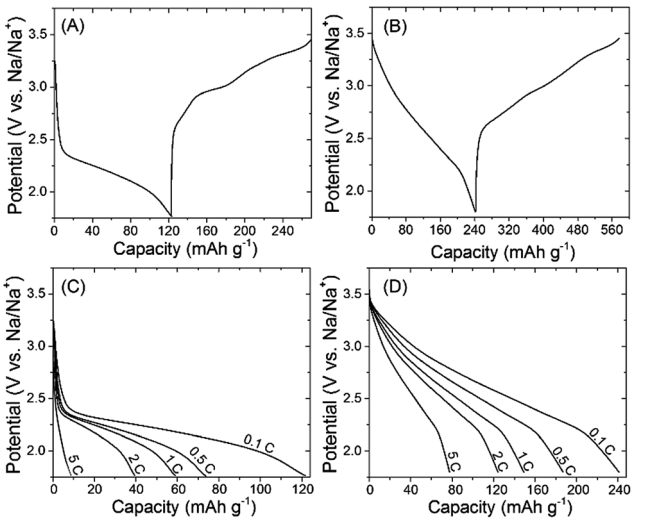

Fig. 3 (a) Charge–discharge curves for the (a) crystalline (450 °C air), and (b) amorphous (180 °C vac) V_2O_5 against Na/Na^+ at a current density of 23.6 mA g^{-1} (0.1 C); the rate capability of the (c) crystalline (450 °C air), and (d) amorphous (180 °C vac) V_2O_5 when discharged at current densities ranging from 23.6 (0.1 C) to 1170 mA g^{-1} (5 C).

density.[16] These effects work to improve the charge and ionic transfer, respectively, at the electrode–electrolyte interface during the sodiation process.

Crystalline transition metal oxides have been the primary framework investigated for ionic-based storage applications, because of their open, yet ordered, structures that offer ample sites for accommodating guest species during intercalation.[49,50] Moreover, there are multiple Faradic charge storage mechanisms, which can simultaneously contribute to the overall capacity. For layered oxides, these mechanisms either occur at the particle surface or within the interlayer spacing of the material. Surface storage is pseudo-capacitive in nature, and can manifest itself *via* the monolayer adsorption of ions or through surface redox reactions. Intercalation-based storage mechanisms, on the other hand, can ensue with or without an accompanying material phase change during the insertion of the ion into the layered structure.[51]

Previous studies have shown that the character of the discharge profile shows a strong dependence on the particle size and on the degree of order of the electro-active species; more specifically, these factors can be independently correlated to the sloped discharge profile seen here (Fig. 3b).[52–54] For nanoparticles below a critical size, pseudo-capacitive behavior stemming from the fast and reversible Faradaic reactions occurring at or near the particle surface culminates in a sloped discharge profile, occurring over a wide potential window.[55,56] Contrastingly, disordering has been shown to lead to sloped potential profiles, given that there is a wider distribution of intercalation site energies in a disordered material; these discrepancies in the intercalation site energy may be negated by the diminished interaction between the intercalation species and the distribution of the activation barrier varying with the local atomic environment, meaning that the Na-ion diffusivity is more independent of the Na-ion concentration.[16]

For amorphous nanomaterials, it is possible that both the nano-based pseudo-capacitive and amorphous-based homogeneous disorder effects can contribute toward the sloped discharge profile. It may be possible to distinguish between these two effects in amorphous materials by synthesizing crystalline nanoparticles of equivalent morphology over a decremental size range and by then monitoring the cyclic voltammetry (CV) for the attenuation of any redox peaks and the adoption of a rectangular CV profile, which is a characteristic trait of pseudo-capacitive storage. Regardless, the obtained results indicate that Na-ion insertion/extraction in amorphous V_2O_5 is not accompanied by an abrupt phase change or alteration of the structure, as is seen in its crystalline equivalent; this attribute ultimately supports the improved cycling stability and makes it possible for the potential to serve as a direct read of the depth of discharge.

CV was accordingly performed to elucidate the redox processes at play for V_2O_5 in its amorphous and crystalline states, the results of which are shown in Fig. 4a, as well as in Fig. S5.† The test cells were successively probed at sweep rates of 0.1, 0.5, and 1.0 mV s^{-1} and within a voltage window of 3.8–1.5 V *vs.* Na/Na^+. The amorphous material did not exhibit any peaks over the CV scan, but the current response marginally scaled with the potential and was greater than the equivalent for the crystalline material; such CV performance is tied to the broad energy dispersion of the sodiation sites, occupied through a percolation mechanism, that gives way to a wide distribution of redox events.[57] Conversely, the CV scans for the crystalline V_2O_5 showed broad anodic peaks, ranging between 3.2 and 3.3 V. When paired with the discharge profiles, these results clearly highlight how the structural differences between the amorphous and crystalline phases can directly impact the Faradaic processes at play.

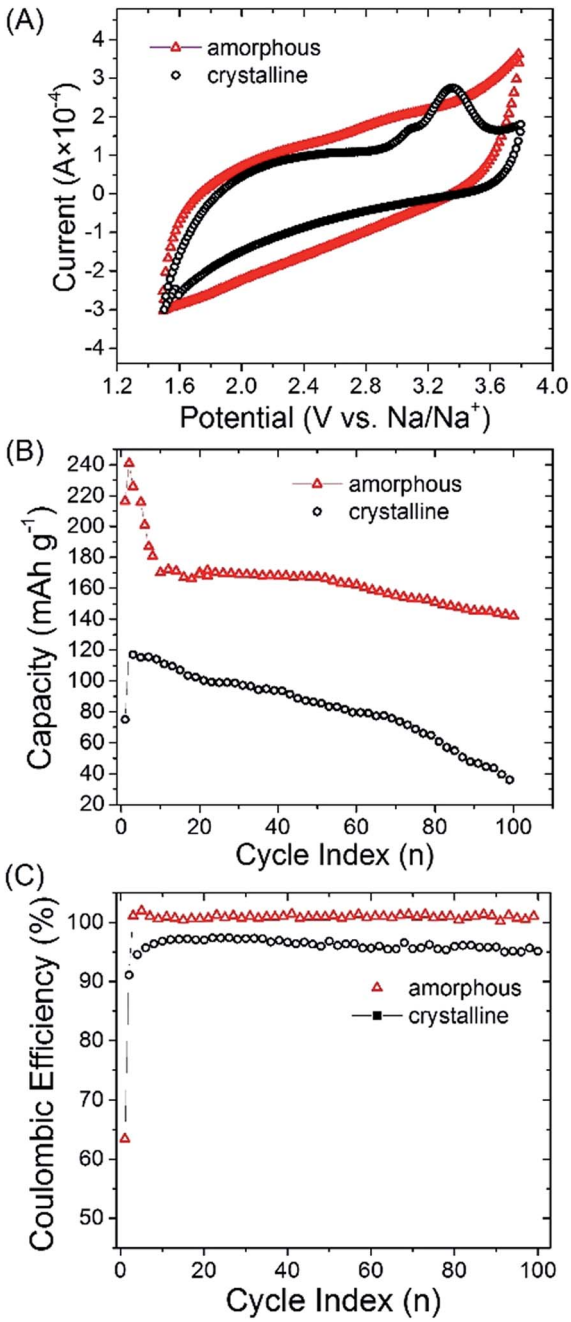

Fig. 4 (a) Cyclic voltammograms for the amorphous (180 °C vac) and crystalline (450 °C air) V_2O_5 at 1.0 mV s^{-1}; (b) the cycle stability; and (c) coulombic efficiency gathered at a current density of 23.6 mA g^{-1}.

The cycle stability and coulombic efficiency of the half-cells was examined at a 0.1 C discharge rate, the results of which are shown in Fig. 4b and c, respectively. The amorphous V_2O_5 material exhibited an initial discharge capacity of 216 mA h g^{-1}, but increased to 241 mA h g^{-1} with the second cycle. However, there was a drop in capacity following this peak, which eventually stabilized at approximately 160 mA h g^{-1}. Similarly, the crystalline V_2O_5 material showed an increase in capacity following the initial cycle and peaked in the second cycle at 120 mA h g^{-1}, but then experienced steady capacity degradation throughout the cycling process, which increased towards the end of the cycling. One would expect these results to be attributed to differences in the ionic diffusivity, based on the characteristic pore discrepancies as induced by the different annealing profiles; however, these differences, as determined from nitrogen sorption analysis, were negligible. Thus, it can be surmised that the disparity in electrochemical performance is directly correlated to the differences in crystallinity, or the apparent lack thereof, and the associated ionic insertion/reaction and diffusion processes. It is worth mentioning that when reproduced, the capacity values can vary slightly, given the non-monotonous cycle stability behavior, but the overall trends hold true.

Given these findings, the use of amorphous V_2O_5 with short-range order has proven to be beneficial for Na-ion battery performance, at least when compared to its crystalline counterpart. The discrepancy in performance is primarily accredited to the low entropic energy associated with the ordering of intercalated atoms and the more open framework. The less structured and more open channels reduce the diffusion barrier for sodium ions to transition between sites, leading to a high rate capability and energy density. The amorphous surface may also make it possible for the sodium ions to more easily penetrate the crystal, thereby diffusing deeper into the material. These effects can lead to a larger capacity at higher current densities, since more of the electro-active material can be infiltrated more rapidly, which ultimately supports the further development and optimization of amorphous electrode materials for future sodium-ion battery application.

Conclusions

In summary, amorphous V_2O_5 electrodes have unambiguously demonstrated that their sodiation capacity, energy density, and cyclic stability are far better than their crystalline contemporaries. The amorphous V_2O_5 electrode, with short range order and a more open framework, demonstrated a discharge capacity of 241 mA h g^{-1} when examined as a positive electrode material for Na-ion battery application, while its crystalline counterpart only had a capacity of 120 mA h g^{-1}. The significant difference between the crystalline and amorphous phases arises from the fast Faradaic reactions that occur in amorphous V_2O_5, stemming from the percolated diffusion network. Moreover, because diffusion now occurs through isotropic percolation and is not confined along a preferential pathway, the overall charging–discharging rates are much faster, as evidenced by the 78 mA h g^{-1} capacity at a current density of 1180 mA g^{-1}. Given these results, the investigation of amorphous electrode materials is expected to be a promising development, and worthy of further research towards yielding high energy density and cycle-life rechargeable sodium batteries.

Acknowledgements

This research work has been financially supported in part by the National Science Foundation (NSF, CMMI-1030048) and the University of Washington TGIF grant. Portions of this work were performed at GeoSoilEnviroCARS (Sector 13), Advanced Photon Source (APS), Argonne National Laboratory. GeoSoilEnviroCARS, which is supported by the National Science Foundation – Earth Sciences (EAR-1128799) and Department of Energy – GeoSciences (DE-FG02-94ER14466). The use of the Advanced Photon Source was supported by the U. S. Department of Energy, Office of Science, Office of Basic Energy Sciences, under Contract no. DE-AC02-06CH11357. We appreciate Tim Fister's help in acquiring the XAS data. Part of this work was conducted at the University of Washington NanoTech User Facility, which is a member of the NSF National Nanotechnology Infrastructure Network (NNIN). This material is based in part upon work supported by the State of Washington through the University of Washington Clean Energy Institute.

Notes and references

1 J. B. Goodenough and K.-S. Park, *J. Am. Chem. Soc.*, 2013, **135**, 1167–1176.
2 V. Etacheri, R. Marom, R. Elazari, G. Salitra and D. Aurbach, *Energy Environ. Sci.*, 2011, **4**, 3243–3262.
3 L. Shen, H. Li, E. Uchaker, X. Zhang and G. Cao, *Nano Lett.*, 2012, **12**, 5673–5678.
4 Q. Zhang, E. Uchaker, S. L. Candelaria and G. Cao, *Chem. Soc. Rev.*, 2013, **42**, 3127–3171.
5 Y.-G. Guo, J.-S. Hu and L.-J. Wan, *Adv. Mater.*, 2008, **20**, 2878–2887.
6 B. Scrosati and J. Garche, *J. Power Sources*, 2010, **195**, 2419–2430.
7 V. Palomares, P. Serras, I. Villaluenga, K. B. Hueso, J. Carretero-Gonzalez and T. Rojo, *Energy Environ. Sci.*, 2012, **5**, 5884–5901.
8 S.-W. Kim, D.-H. Seo, X. Ma, G. Ceder and K. Kang, *Adv. Energy Mater.*, 2012, **2**, 710–721.
9 B. L. Ellis and L. F. Nazar, *Curr. Opin. Solid State Mater. Sci.*, 2012, **16**, 168–177.
10 N. Hudak and D. Huber, *ECS Trans.*, 2011, **33**, 1–13.
11 M. D. Slater, D. Kim, E. Lee and C. S. Johnson, *Adv. Funct. Mater.*, 2013, **23**, 947–958.
12 M. Mikkor, *J. Electrochem. Soc.*, 1985, **132**, 991–998.
13 Y. Kim, Y. Park, A. Choi, N. S. Choi, J. Kim, J. Lee, J. H. Ryu, S. M. Oh and K. T. Lee, *Adv. Mater.*, 2013, **25**, 3045–3049.
14 S. P. Ong, V. L. Chevrier, G. Hautier, A. Jain, C. Moore, S. Kim, X. Ma and G. Ceder, *Energy Environ. Sci.*, 2011, **4**, 3680–3688.
15 H. Xiong, M. D. Slater, M. Balasubramanian, C. S. Johnson and T. Rajh, *J. Phys. Chem. Lett.*, 2011, **2**, 2560–2565.

16 J. Lee, A. Urban, X. Li, D. Su, G. Hautier and G. Ceder, *Science*, 2014, **343**, 519–522.
17 H.-T. Fang, M. Liu, D.-W. Wang, T. Sun, D.-S. Guan, F. Li, J. Zhou, T.-K. Sham and H.-M. Cheng, *Nanotechnology*, 2009, 20.
18 G. Venkatesh, V. Pralong, O. I. Lebedev, V. Caignaert, P. Bazin and B. Raveau, *Electrochem. Commun.*, 2014, **40**, 100–102.
19 J. Haber, *Catal. Today*, 2009, **142**, 100–113.
20 C. Delmas, H. Cognacauradou, J. M. Cocciantelli, M. Menetrier and J. P. Doumerc, *Solid State Ionics*, 1994, **69**, 257–264.
21 Z. J. Lao, K. Konstantinov, Y. Tournaire, S. H. Ng, G. X. Wang and H. K. Liu, *J. Power Sources*, 2006, **162**, 1451–1454.
22 J. D. Jarrell, B. Dolly and J. R. Morgan, *J. Biomed. Mater. Res., Part A*, 2009, **90A**, 272–281.
23 Y. Wang and G. Z. Cao, *Chem. Mater.*, 2006, **18**, 2787–2804.
24 Y. Liu, E. Uchaker, N. Zhou, J. Li, Q. Zhang and G. Cao, *J. Mater. Chem.*, 2012, **22**, 24439–24445.
25 E. Uchaker, N. Zhou, Y. Li and G. Cao, *J. Phys. Chem. C*, 2013, **117**, 1621–1626.
26 E. Uchaker, M. Gu, N. Zhou, Y. Li, C. Wang and G. Cao, *Small*, 2013, **9**, 3880–3886.
27 S. Tepavcevic, H. Xiong, V. R. Stamenkovic, X. Zuo, M. Balasubramanian, V. B. Prakapenka, C. S. Johnson and T. Rajh, *ACS Nano*, 2012, **6**, 530–538.
28 D. Su and G. Wang, *ACS Nano*, 2013, **7**, 11218–11226.
29 H. Liu, H. Zhou, L. Chen, Z. Tang and W. Yang, *J. Power Sources*, 2011, **196**, 814–819.
30 Z. Chen, V. Augustyn, X. Jia, Q. Xiao, B. Dunn and Y. Lu, *ACS Nano*, 2012, **6**, 4319–4327.
31 D. Liu, Y. Liu, A. Pan, K. P. Nagle, G. T. Seidler, Y.-H. Jeong and G. Cao, *J. Phys. Chem. C*, 2011, **115**, 4959–4965.
32 Y. Y. Liu, J. G. Li, Q. F. Zhang, N. Zhou, E. Uchaker and G. Z. Cao, *Electrochem. Commun.*, 2011, **13**, 1276–1279.
33 C. J. Fontenot, J. W. Wiench, M. Pruski and G. L. Schrader, *J. Phys. Chem. B*, 2000, **104**, 11622–11631.
34 M. Nabavi, C. Sanchez and J. Livage, *Philos. Mag. B*, 1991, **63**, 941–953.
35 J.-H. Huang, Q.-Y. Lai, J.-M. Song, L.-M. Chen and X.-Y. Ji, *Chin. J. Inorg. Chem.*, 2007, **23**, 237–242.
36 A. Z. Moshfegh and A. Ignatiev, *Thin Solid Films*, 1991, **198**, 251–268.
37 J. L. C. Sanchez and G. Lucazeau, *J. Raman Spectrosc.*, 1982, **12**, 68–72.
38 Y. Wang, K. Takahashi, K. Lee and G. Cao, *Adv. Funct. Mater.*, 2006, **16**, 1133–1144.
39 P. Aldebert, N. Baffier, N. Gharbi and J. Livage, *Mater. Res. Bull.*, 1981, **16**, 669–676.
40 Y. Wang, H. Shang, T. Chou and G. Cao, *J. Phys. Chem. B*, 2005, **109**, 11361–11366.
41 N. Ozer, *Thin Solid Films*, 1997, **305**, 80–87.
42 M. Benmoussa, E. Ibnouelghazi, A. Bennouna and E. L. Ameziane, *Thin Solid Films*, 1995, **265**, 22–28.
43 C. W. Zou, X. D. Yan, J. Han, R. Q. Chen and W. Gao, *J. Phys. D: Appl. Phys.*, 2009, **42**, 145402.
44 B. Ravel and M. Newville, *J. Synchrotron Radiat.*, 2005, **12**, 537–541.
45 A. N. Mansour, S. Dallek, P. H. Smith and W. M. Baker, *J. Electrochem. Soc.*, 2002, **149**, A1589.
46 A. N. Mansour, P. H. Smith, W. M. Baker, M. Balasubramanian and J. McBreen, *J. Electrochem. Soc.*, 2003, **150**, A403.
47 W. Avansi, L. J. Q. Maia, C. Ribeiro, E. R. Leite and V. R. Mastelaro, *J. Nanopart. Res.*, 2011, **13**, 4937–4946.
48 G. Silversmit, J. A. van Bokhoven, H. Poelman, A. M. J. van der Eerden, G. B. Marin, M.-F. Reyniers and R. De Gryse, *Appl. Catal., A*, 2005, **285**, 151–162.
49 M. S. Whittingham, *Chem. Rev.*, 2004, **104**, 4271–4301.
50 M. S. Whittingham, *Science*, 1976, **192**, 1126–1127.
51 V. Augustyn, J. Come, M. A. Lowe, J. W. Kim, P.-L. Taberna, S. H. Tolbert, H. D. Abruna, P. Simon and B. Dunn, *Nat. Mater.*, 2013, **12**, 518–522.
52 M. Wagemaker, W. J. H. Borghols, E. R. H. van Eck, A. P. M. Kentgens, G. L. Kearley and F. M. Mulder, *Chem.–Eur. J.*, 2007, **13**, 2023–2028.
53 J. P. J. Wang, T. Brezesinski, S. Tolbert and B. Dunn, *ECS Trans.*, 2008, **11**, 101–111.
54 J. W. Kim, V. Augustyn and B. Dunn, *Adv. Energy Mater.*, 2012, **2**, 141–148.
55 P. Simon and Y. Gogotsi, *Nat. Mater.*, 2008, **7**, 845–854.
56 B. E. Conway, *J. Electrochem. Soc.*, 1991, **138**, 1539–1548.
57 P. Balaya, A. J. Bhattacharyya, J. Jamnik, Y. F. Zhukovskii, E. A. Kotomin and J. Maier, *J. Power Sources*, 2006, **159**, 171–178.

